

Probing the magnetospheric accretion region of the young pre-transitional disk system DoAr 44 using VLTI/GRAVITY[★]

J. Bouvier¹, K. Perraut¹, J.-B. Le Bouquin¹, G. Duvert¹, C. Dougados¹, W. Brandner², M. Benisty^{1,3}, J.-P. Berger¹, and E. Alécian¹

¹ Univ. Grenoble Alpes, CNRS, IPAG, 38000 Grenoble, France
e-mail: Jerome.Bouvier@univ-grenoble-alpes.fr

² Max Planck Institute for Astronomy, Königstuhl 17, 69117 Heidelberg, Germany

³ Unidad Mixta Internacional Franco-Chilena de Astronomía (CNRS, UMI 3386), Departamento de Astronomía, Universidad de Chile, Camino El Observatorio 1515, Las Condes, Santiago, Chile

Received 29 January 2020; accepted 24 March 2020

ABSTRACT

Context. Young stellar objects are thought to accrete material from their circumstellar disks through their strong stellar magnetospheres.

Aims. We aim to directly probe the magnetospheric accretion region on a scale of a few 0.01 au in a young stellar system using long-baseline optical interferometry.

Methods. We observed the pre-transitional disk system DoAr 44 with VLTI/GRAVITY on two consecutive nights in the K-band. We computed interferometric visibilities and phases in the continuum and in the Bry line in order to constrain the extent and geometry of the emitting regions.

Results. We resolve the continuum emission of the inner dusty disk and measure a half-flux radius of 0.14 au. We derive the inclination and position angle of the inner disk, which provides direct evidence that the inner and outer disks are misaligned in this pre-transitional system. This may account for the shadows previously detected in the outer disk. We show that Bry emission arises from an even more compact region than the inner disk, with an upper limit of 0.047 au ($\sim 5 R_*$). Differential phase measurements between the Bry line and the continuum allow us to measure the astrometric displacement of the Bry line-emitting region relative to the continuum on a scale of a few tens of microarcsec, corresponding to a fraction of the stellar radius.

Conclusions. Our results can be accounted for by a simple geometric model where the Bry line emission arises from a compact region interior to the inner disk edge, on a scale of a few stellar radii, fully consistent with the concept of magnetospheric accretion process in low-mass young stellar systems.

Key words. Stars: pre-main sequence – Stars: variables: T Tauri – Stars: magnetic field – Accretion, accretion disks – Stars: individual: DoAr 44

1. Introduction

During the first few million years, the young low-mass stellar systems known as T Tauri stars are surrounded by a circumstellar disk from which they accrete material. In the inner disk region, at a distance of a few stellar radii above the stellar surface, the strong stellar magnetic field is able to disrupt the radial accretion flow, which is then forced to follow the magnetic field lines down to the stellar surface (Bouvier et al. 2007b; Hartmann et al. 2016). Magnetic funnel flows thus develop, connecting the inner disk edge to the stellar surface on a scale of a few 0.01 au. At the distance of the nearest star forming regions (≥ 100 pc), the angular size of the star-disk interaction region is therefore of the order of a milli-arcsec (mas) or less, a scale barely reachable with even the largest telescopes. This is the reason why the magnetospheric accretion process in T Tauri stars has been investigated mostly indirectly so far, for example, by monitoring the variability of the inner system as it rotates (e.g., Bouvier et al. 2007a; Alencar et al. 2012, 2018; Donati et al. 2019). However, interferomet-

ric facilities offer the promise to reach these scales (Eisner et al. 2009, 2010, 2014), and the spectacular improvement in sensitivity and stability of newly available interferometric near-infrared instruments now allows us to directly probe the accretion flows within the magnetosphere of young stellar systems. We report here such an attempt using GRAVITY at the VLTI (Gravity Collaboration et al. 2017a).

We performed a large-scale, multi-instrument campaign in June 2019, monitoring the young pre-transitional disk system DoAr 44 (aka V2062 Oph, Haro 1-16, ROXs 44, HBC 268). This young stellar object is a 1.2 M_{\odot} classical T Tauri star (cTTS) located in the Rho Ophiuchus dark cloud at a distance of 146 ± 1 pc (Gaia Collaboration et al. 2016, 2018). A moderately bright source of spectral type K3, it exhibits strong H α emission ($EW(H\alpha) \approx 50 \text{ \AA}$, Bouvier & Appenzeller 1992) and accretes at a substantial rate from its circumstellar disk ($\dot{M}_{\text{acc}} = 6.0\text{--}9.3 \cdot 10^{-9} M_{\odot} \text{ yr}^{-1}$, Espaillat et al. 2010; Manara et al. 2014). From the measurement of Zeeman broadening of near-infrared FeI lines, Lavail et al. (2017) derived a mean surface magnetic field strength amounting to 1.8 ± 0.4 kG, and possibly up to 3.6 kG. The moderate mass accretion rate and strong magnetic field

[★] Based on observations collected at the European Organisation for Astronomical Research in the Southern Hemisphere under ESO programme 0103.C-0097

makes DoAr 44 a prime target to investigate the magnetospheric accretion process in this system.

The overall results of the multi-instrument campaign are reported in an accompanying paper (Bouvier et al., in prep.; hereafter Paper I). Here, we present and analyze the unique datasets obtained from long baseline optical interferometry, using VLTI/GRAVITY. Section 2 describes the observations. Section 3 presents the analysis of the interferometric visibilities and phases both in the K-band continuum and across the Bry emission-line profile. Section 4 provides an interpretation of the results in terms of a simple geometrical model for the star-disk interaction region in this system, based on the interferometric observables.

2. Observations

We observed DoAr 44 on June 22 and 23, 2019 in the K-band with the GRAVITY instrument (Gravity Collaboration et al. 2017a), combining the four unit telescopes of the ESO/VLTI (ESO run 60.A-9256). At $2.2 \mu\text{m}$, with a maximum baseline of 130 m, we thus reach an angular resolution of $\lambda/2B_{\text{max}} = 1.7 \text{ mas}$, corresponding to 0.25 au at 146 pc. After the MACAO adaptive optics correction, the flux of the source is split and feeds the fringe tracker and science instrument simultaneously. We collected exposures with coherent integrations of 0.85 ms on the fringe tracker to freeze the atmospheric effects (Lacour et al. 2019). Once the fringes were stabilized, we recorded successive sequences of 5 minutes, namely 10 exposures of 30 s each, on the object with the science instrument in its high spectral resolution mode ($R \sim 4,000$). The datasets thus consist of long sequences of integration on DoAr 44, interleaved with sky exposures and interferometric calibrator observations. The calibrators were chosen to be unresolved at the longest baselines, located close to the target on the sky, and having a similar magnitude in the K band. Several calibrators were observed in order to derive the instrumental transfer function accurately. Weather conditions were excellent during the first night and we recorded 26 files of five minutes each over a period of 3.7 hours. At the start of the second night, we recorded only one hour of exploitable data, as the domes had to be closed to high winds thereafter. The journal of observations is given in Table 1.

3. Results

We report in this section the data reduction processes that allowed us to measure interferometric visibilities and phases along the six baselines sampled by the four ESO/VLTI unit telescopes. From these measurements, we derive the main properties of the emitting regions, both in the continuum and across the Bry line profile.

3.1. Continuum visibilities

We used the standard GRAVITY pipeline (Gravity Collaboration et al. 2017a; Lapeyrere et al. 2014) to reduce the fringe tracker data. Complex visibilities were computed over five spectral channels and were used to constrain the extent of the K-band continuum emitting region. Since the error bars provided by the pipeline can be underestimated and/or do not include the residual calibration effects, we adopted conservative error bars: for the squared visibilities, we computed the rms over exposures probing the same spatial frequencies, which yields error bars amounting to 2% in all spectral channels; for the closure phases,

we computed the rms over the 36 exposures recorded during the two nights and derived an rms of 0.8° when considering all the spectral channels, and of 0.3° when considering the central spectral channel only. The squared visibilities can be fit as a function of the baseline with geometrical models, while the closure phase measures the degree of asymmetry of the emitting region (e.g., Monnier 2007). Figure 1 displays results from the dataset obtained on June 22, 2019. The K-band continuum-emitting region of DoAr 44 appears to be partially resolved ($V^2 < 1$) and centrosymmetric as suggested by a closure phase close to 0° . The results obtained from the observations performed on June 23, 2019 are consistent with the results of the first night but do not significantly add to the signal to noise of the visibilities or phases due to their limited duration.

To model the visibilities, we followed the approach Lazareff et al. (2017) and Gravity Collaboration et al. (2019) applied to the analysis of interferometric surveys of Herbig stars performed with PIONIER and GRAVITY, respectively. For the continuum K-band emitting region, we fit the visibility measurements as a function of baseline with a three component model: a point-like central star (since we are not able to resolve the stellar photosphere), a circumstellar disk that is modeled as a 2D elliptical Gaussian, and an extended component. The latter contribution, also called halo in Lazareff et al. (2017), is assumed to be fully resolved, leading to visibilities smaller than 1 at very short baselines. This extended component contribution is sometimes interpreted as scattered light (Pinte et al. 2008). Indeed, it has been found to improve the parametric modeling of young stellar objects for which the scattered light flux is significant, mainly transitional disks (Lazareff et al. 2017) and T Tauri stars (Anthonioz et al. 2015). The free parameters are the relative contributions to the total flux of the star f_s , the circumstellar disk f_c , and the extended component (if any) f_h , with the sum of these contributions being equal to unity, the half-flux semi-major axis, the inclination, and the position angle of the circumstellar disk. The total complex visibility at the spatial frequency (u, v) and wavelength λ is given by:

$$V(u, v, \lambda) = \frac{f_s(\lambda) + f_c(\lambda)V_c(u, v)}{f_s(\lambda) + f_c(\lambda) + f_h(\lambda)}, \quad (1)$$

where V_c denotes the visibility of the circumstellar disk, and the wavelength dependence of the flux contributions is explained in Lazareff et al. (2017)¹.

Since the disk is only partially resolved by our observations, its flux contribution f_c and half-flux radius are partly degenerated (Lazareff et al. 2017). We used the K-band excess ratio $F_{\text{exc}}/F_\star = 0.8 \pm 0.2$ measured by Espaillat et al. (2010) from the spectral energy distribution of the system to derive a starting value for f_c but kept it as a free parameter for the visibility fit. The flux contributions we derive for the different components indicate that, at the time of our observations, the star dominated the continuum emission in the K-band, with a disk fractional flux f_c ranging from 20 to 34%. The best fit model yields $F_{\text{exc}}/F_\star = 0.49 \pm 0.12$, where the difference from Espaillat et al. (2010) estimate may reflect intrinsic variability of the system over a timescale of years. The visibilities corresponding to the best fit model do not reach unity at zero baseline, which is interpreted as the presence of an additional, fully resolved extended component that contributes about 6-7% to the total flux of the system in the K-band. The results of the best-fit model are listed in Table 2. The $1-\sigma$ errors

¹ The chromatic exponents from Lazareff et al. (2017) model amount to $k_s = 1.1$ and $k_c = -0.2$ in our best fit model.

Table 1. Journal of the VLTI/GRAVITY observations. N denotes the number of five-minute-long sequences that have been recorded on the target.

HJD	Date	Time (UT)	Configuration	N	Seeing (")	τ_0 (ms)	Calibrators
2458656.66339	2019-06-22	02:04 - 05:46	UT1-UT2-UT3-UT4	26	0.41 - 0.88	6.4 - 15.8	HD 147578, HD 149562
2458657.59764	2019-06-23	01:48 - 02:50	UT1-UT2-UT3-UT4	10	0.84 - 1.16	6.8 - 9.7	HD 146706, HD 146235

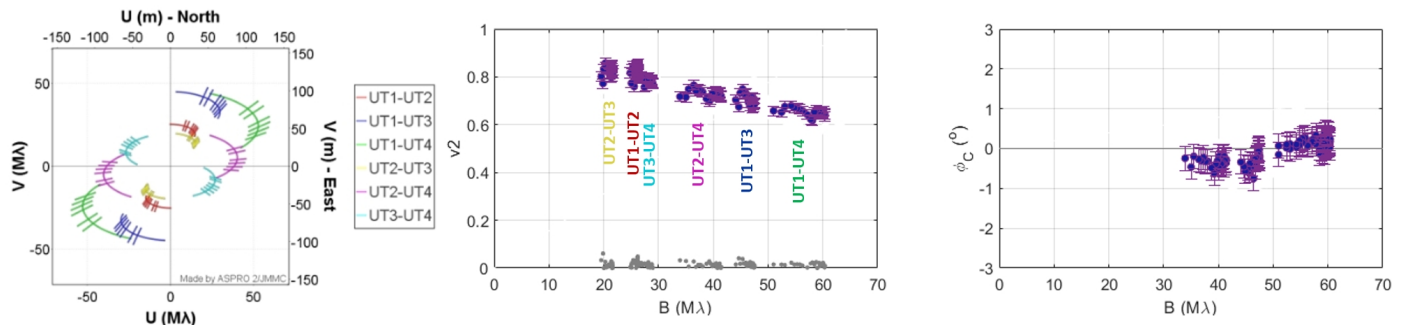

Fig. 1. GRAVITY observations of DoAr 44 on June, 22. *Left:* (u, v) spatial frequency plane corresponding to the six projected baselines during the 3.7 hours of observations. *Middle:* continuum squared visibilities as a function of baseline, recorded in the central spectral channel of the fringe tracker ($\lambda = 2.15 \mu\text{m}$). The gray circles at the bottom of the panel correspond to the residuals after the best fit model has been subtracted (see text). *Right:* closure phases measured in the central spectral channel as a function of baseline. The error bars amount to 2% on the squared visibilities and 0.3° on the closure phases (see text for details).

Table 2. Best-fit parameters of the K-band continuum VLTI/GRAVITY data of DoAr 44 obtained on June 22, 2019. See text for a detailed description of the model.

Parameters	Ellipsoid
f_c	0.27 ± 0.07
f_h	0.06 ± 0.01
f_s	0.67 ± 0.07
$\cos i$	0.83 ± 0.02
PA [$^\circ$]	140 ± 3
Half-flux radius [mas]	0.96 ± 0.18
Half-flux radius [au]	0.14 ± 0.026
Half-flux radius [R_\star]	15.0 ± 2.8
χ_r^2	1.06

are provided for all the parameters, and take into account the partial degeneracy between the disk fractional flux and the half-flux radius.

The model converges towards a 2D elliptical Gaussian whose minor-to-major-axis ratio is equal to 0.83, corresponding to an inclination of 34° , at a position angle of 140° measured east from north. The mean half-flux radius of 0.96 mas corresponds to 0.14 au ($\sim 15 R_\star$)² at a distance of 146 pc. We checked that the data obtained on the second night, in spite of their lower quality, are in agreement with these parameters. We also checked that a ring model converges towards the same values of parameters, which indicates that we are not able to resolve an inner cavity at the scale of our angular resolution.

² The stellar radius, $R_\star = 2.0 \pm 0.15 R_\odot$, was obtained in Paper I from the luminosity and T_{eff} we derived for the star.

3.2. $\text{Br}\gamma$ line interferometric observables

The spectrally dispersed observations from the science instrument (SC) were reduced with the latest version of the instrument pipeline. It includes recent fixes to lower the imprint of the internal source in the calibration frames, and a better filtering of the outliers created by cosmic rays. As a sanity check, we reduced the SC data with four independent sets of calibration files, recorded on June 18, 20, 22, and 27. We obtained consistent results for all of them.

The calibrator observations were somewhat noisier than the science data, due to the limited number of calibration sequences. We therefore did not perform an absolute calibration of the spectrally dispersed observations, as this would have degraded the signal-to-noise ratio of the science data. Instead, we used differential measures that can be reliably computed by renormalizing the spectrally dispersed data, forcing the continuum around the $\text{Br}\gamma$ line to match the prediction of the best-fit model of the continuum emission derived from the calibrated FT data (see Sec. 3.1). We averaged all observations for each of the two nights in order to increase the signal-to-noise ratio. The subsequent uv -plane smearing has no significant impact on the results because the relevant scales are marginally resolved. The spectrally dispersed interferometric observables are shown in Figure A.1. The first night has typical standard deviations of 0.004 in visibility amplitude, 0.25° in phase for each baseline, and 0.45° in phase closures, while the second is of lower quality, with $1-\sigma$ uncertainties of 0.01 in amplitude, 0.5° in phase, and 0.8° in phase closures.

The $\text{Br}\gamma$ line appears in emission in the spectrum. Its measured FWHM is 1.25 nm, therefore slightly enlarged compared to the 0.40 nm spectral resolution of GRAVITY. This broadening corresponds to a velocity dispersion of 164 km s^{-1} . An increase of visibility amplitude is seen across the line profile for all baselines. A small but consistent signal is also seen in the differential phase across the line profile along three baselines over the two nights (see Fig. A.1). It reaches a level of 2.2, 2.5, and 3.3σ along baselines UT4-3/2/1, respectively, for the first night.

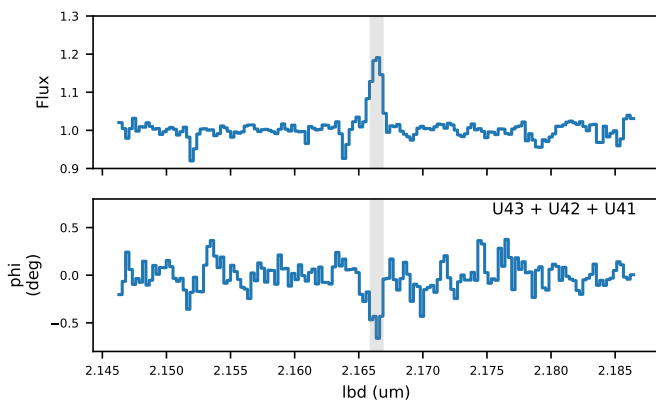


Fig. 2. *Top panel:* Spectrum around the Br γ line for the night 2019-06-22. The gray area shows the extent of the Br γ line profile. *Bottom panel:* Mean of the differential phase of the three baselines UT4-UT3, UT4-UT2, and UT4-UT1 for the night 2019-06-22. The standard deviation of the summed signal is 0.16° . The averaged phase signal is detected across the line profile at the 4σ level.

Table 3. Best-fit parameters of the Br γ VLTI/GRAVITY data of DoAr 44. The errors are $1\text{-}\sigma$ uncertainties.

Parameters	2019-06-22	2019-06-23
$F_{\text{Br}\gamma} / F_{\text{cont}}$	0.19 ± 0.02	0.17 ± 0.02
Half-flux radius [mas]	< 0.32	< 0.25
Half-flux radius [au]	< 0.047	< 0.037
Half-flux radius [R_\star]	< 5.0	< 3.9
Offset [μas]	52 ± 15	67 ± 55
PA [$^\circ$]	163 ± 15	158 ± 50

When averaging the three baselines, the signature appears at the 4σ level across the line profile, as shown in Figure 2. There is no significant detection of a phase closure signal across the Br γ line at a 1σ level of 0.31, 0.43, 0.31, 0.25 deg for the first night. The signatures of all interferometric observables across the line profile are adequately modeled by a Gaussian, with no evidence for a more complicated spectral profile (e.g., double peaked or S-shaped), and the behavior of interferometric observable is the same for the two nights.

The simplest geometrical model able to account for such signatures is a compact, mostly unresolved Br γ emission region. It is hereafter described by a Gaussian, without spatially resolved kinematics, which is slightly offset with respect to the barycenter of the continuum emission. In addition to the Br γ line position, broadening, and flux, the free parameters of the model are the angular half-flux radius of the Br γ emitting region, its astrometric offset relative to the continuum emission, and the position angle of this offset. While adjusting the spectrally dispersed data with the model, we kept the parameters of the continuum fixed since they are constrained by the FT data onto which the continuum has been rescaled. The best-fit model is overlaid to the data in Figure A.1, and the corresponding best-fit parameters are listed in Table 3.

The Br γ emitting region is not spatially resolved. The upper limit of 0.32 mas we derive on its size corresponds to 0.047 au at a distance of 146 pc, which translates into $5 R_\star$, for a stellar radius of $2 R_\odot$, as derived in Paper I. The Br γ line emitting region is thus significantly more compact than the inner circumstellar disk whose half-flux radius reaches $15 R_\star$. The astrometric offset measures the distance between the photocenter of the Br γ

emitting region and that of the continuum. It is listed in Table 3 and is expressed in microarcseconds, illustrating the exquisite precision of differential near-infrared long baseline interferometry. For the first night, the offset value of $52 \mu\text{as}$ corresponds to 0.0076 au, meaning $0.82 R_\star$, at a position angle of about 160° . The poorer signal-to-noise ratio gathered during the second night unfortunately prevents us from detecting any temporal evolution of either the amplitude or the position angle of the astrometric offset.

4. Discussion

DoAr 44 belongs to the class of relatively rare young stellar systems with pre-transitional circumstellar disks. On large scales, high angular resolution $880 \mu\text{m}$ continuum maps obtained with SMA by Andrews et al. (2009, 2011) reveal the existence of a dust-depleted cavity extending up to a distance of 30 au from the central star with the cold dust emission arising from an outer ring about 25 au-wide. ALMA observations in the optically thin ^{13}CO and C^{18}O lines reveal a ring structure similar to that seen in the dust continuum emission albeit somewhat wider, namely a rotating gaseous ring extending from about 25 to 60 au from the central star, seen at an inclination of $\approx 20^\circ$ (van der Marel et al. 2016). In addition, adaptive optics H-band polarized images reveal the presence of two symmetric shadows in the azimuthal brightness profile of the outer ring seen in scattered light (Casasus et al. 2018). A radiative transfer model suggests that these shadows are cast by an inner disk warp, with a relative inclination amounting to $30 \pm 5^\circ$ between the inner disk and the outer ring. On small scales, Espaillat et al. (2010) ascribed the near-infrared excess observed in the spectral energy distribution of the source to a hotter dust component, located at the dust sublimation radius of an optically thick inner disk. Using a radiative transfer model to describe the inner disk wall, they deduce a dust sublimation radius of 0.25 au at a temperature of 1200 K, and a size less than 0.4 au for the inner disk. Salyk et al. (2009, 2011) investigated the inner disk gaseous component by modeling the rovibrational transitions of CO lines seen in emission in the near-IR spectrum of the source. They derived a gaseous disk inner radius of 0.3 ± 0.1 au, which is consistent with that of the dusty component responsible for the near-IR excess. Thus, pre-transitional disk systems consist of a compact inner disk close to the star surrounded by a wide gas and dust-depleted cavity, and an outer ring or disk component, with a possible misalignment between the inner and outer scales of the circumstellar material.

Near-IR spectro-interferometry and spectro-astrometry are powerful tools to explore the innermost regions of young stellar objects surrounded by circumstellar disks (e.g. Malbet et al. 2007; Kraus et al. 2008; Goto et al. 2012; Eisner et al. 2014; Mendigutía et al. 2015; Gravity Collaboration et al. 2017b, 2019, 2020). Indeed, our long baseline optical interferometric observations allow us to directly constrain the properties of the inner system. The inner dusty disk of DoAr 44 is resolved in our GRAVITY data with a half-flux radius of 0.14 au, corresponding to $\sim 15 R_\star$. This is nearly a factor of two more compact than the location of the 1200 K inner dust wall inferred by Espaillat et al. (2010) to account for the near infrared excess flux of DoAr 44's spectral energy distribution. Given uncertainties attached to the latter estimate, which depends upon the assumed inner wall geometry, the dust properties, and the stellar and accretion properties, the discrepancy might either not be significant or could indicate long-term variations in the extent of the star-disk interaction region. From the fit of the continuum visibilities, we further derive an inclination of $34^\circ \pm 2^\circ$ and a PA of $140^\circ \pm 3^\circ$ for

the inner disk. These values are remarkably consistent with the inclined disk model inferred by Casassus et al. (2018), which requires $i \approx 29.7^\circ$ and $PA \approx 134^\circ$ for the inner disk to account for the location of the shadows seen in the outer dusty ring. Hence, the GRAVITY results presented here seem to provide direct support to the interpretation of shadows seen in the outer circumstellar ring as being due to a misalignment between the inner and outer disks in this pre-transitional disk system.

The larger visibilities we measure across the Bry line profile compared to those computed for the nearby continuum readily indicate that the Bry emitting region is more compact than the inner dusty disk. The model fit of the interferometric visibilities yields an upper limit of 0.047 au, meaning $5 R_\star$, to the Bry line-emitting region. This is typically the size of the magnetospheric accretion region in young stellar systems (e.g., Bouvier et al. 2007b) and quite similar to the corotation radius of 0.043 au ($4.63 R_\star$) we derived for the system in Paper I ($P_{rot} = 2.96$ d). Moreover, the differential phase signal indicates a small but significant astrometric offset between the photocenter of the line-emitting region relative to that of the continuum emission. The offset amounts to 0.0076 and 0.0098 au, corresponding to 0.82 and $1.06 R_\star$, on the first and second nights, respectively, and lies at a position angle of about 160° . Within significant uncertainties (cf. Table 3), the amplitude of the astrometric offset and its position angle may have remained constant over this timescale.

Do these results fit the magnetospheric accretion paradigm for low-mass young stellar objects? The Bry line flux in the spectra of young stars has been shown to diagnose and reliably measure the mass-accretion rate onto the star (e.g., Najita et al. 1996; Muzerolle et al. 1998b). Radiative transfer modeling of line emission arising from magnetospheric funnel flows in an aligned dipolar geometry predicts relatively symmetric Bry line profiles (Muzerolle et al. 1998a). At low inclination, as is relevant for DoAr 44 ($i \approx 30^\circ$, Paper I), the profile does not exhibit conspicuous inverse P Cygni features, and is nearly centered at the star's velocity (Kurosawa et al. 2011). All these properties are consistent with the Gaussian-like, centered Bry line profile we report here at moderate spectral resolution (see Fig. 2).

The near-IR hydrogen line emission is expected to arise from the bulk of the magnetosphere, extending from the disk truncation radius down to the stellar surface (Kurosawa et al. 2008). Assuming the truncation radius is close to the corotation radius, as is often the case for T Tauri stars (e.g., Alencar et al. 2012, 2018; Donati et al. 2013, 2020), we expect Bry emission to arise over a large volume around the star, extending up to about $4.6 R_\star$. This is consistent with the upper limit we derive on the half-flux radius of the Bry line-emitting region from interferometric visibilities (see Table 3).

Even in the case of a slightly misaligned dipole³, line emission from magnetospheric funnel flows remains relatively symmetric at low inclination (see, e.g., model A in Kurosawa et al. 2008). The astrometric offset we measure between the photocenter of the Bry emission region and the center of the stellar disk amounts to a fraction of the stellar radius (0.6-1.1 R_\star , see Appendix B). While a full MHD-radiative transfer model would be required to clarify the origin of such a small offset, we conjecture that it could result from an azimuthal modulation of the funnel flow emission, as expected from accretion, onto a slightly misaligned dipole or a more complex large-scale magnetic topology indeed (e.g., Kurosawa & Romanova 2013).

³ We derive a 20° magnetic obliquity for DoAr 44 in Paper I from Zeeman Doppler Imaging.

Overall, we therefore believe that our results are consistent with the assumption that we might be directly probing the Bry emitting region arising from funnel flows within the stellar magnetosphere of the young DoAr 44 system.

Alternatively, bipolar stellar winds or jet outflows may also be expected to contribute near-IR hydrogen line emission in young stellar systems (e.g., Kurosawa & Romanova 2012), in a direction perpendicular to the disk midplane. However, we find here that the PA of the astrometric offset of the Bry emission is nearly along the disk's major axis, which does not support an interpretation in terms of polar outflows. The base of disk winds is another potential source of Bry emission but it would have to originate here within $5 R_\star$ from the central object. Moreover, rotating disk winds and bipolar outflows alike, yield an S-shape signature in the spectrally dispersed differential interferometric phases across the line profile (e.g., Weigelt et al. 2011; Kreplin et al. 2018), which is not seen here (see Fig. 2).

Finally, more exotic interpretations cannot be ruled out. For instance, part of the Bry emission could arise from an accreting planet orbiting close to the star. Hydrogen emission has been directly detected in the circumstellar disks of young systems at the location of wide-orbit planets (e.g., Haffert et al. 2019). Compact close-in planetary systems, such as those revealed by Kepler with orbital periods of a few days (e.g., Winn et al. 2018), could conceivably yield these kinds of signatures when still embedded in the inner disk. Additional evidence, such as periodic radial velocity variations, would however be required to support this hypothesis. We do detect a periodic modulation of the star's radial velocity in Paper I, with an amplitude of about 0.6 km s^{-1} , but the modulation occurs at the stellar rotation period, which points to stellar activity.

5. Conclusion

Long baseline near-infrared interferometry provides a unique opportunity to get direct constraints on the inner scales of the environment of young stellar objects, down to a few 0.01 au. Its application to the young pre-transitional disk system DoAr 44 has allowed us to derive the properties of the inner disk and to put strong constraints on the origin and size of the Bry line emitting region.

We resolve a compact inner disk on a scale of 0.14 au around the central star, and derive similar inclinations onto the line of sight for the inner disk and the central star, which is different from that of the outer ring seen at much larger scales. This result provides strong support to the interpretation of dark shadows seen in outer rings of pre-transitional disk systems as resulting from inner-outer disk misalignment.

The interferometric observables across the Bry line profile reveal a compact line emitting region, of the order of 0.04 au or less. Thus, both the maximum size of the Bry emitting region, of the order of $5 R_\star$ or less, and its offset from the central star, which amounts to a fraction of the stellar radius, suggest that the Bry emission arises in the funnel flows of the magnetospheric accretion region, located between the inner disk edge at 0.12 au and the stellar surface. Indeed, the maximum size we derive for the Bry line-emitting region is similar to the Keplerian disk's corotation radius, which usually coincides with the radius at which the inner disk is truncated as it encounters the stellar magnetosphere.

Finally, we wish to emphasize that as sharp as it is, the interferometric view of the inner regions of young accreting systems is best exploited when combined with complementary approaches, such as spectropolarimetry, high-resolution spectroscopic monitoring, and multicolor photometry. The interfero-

metric results presented here are further discussed in the context of the full observing campaign on DoAr 44 reported in Paper I. It is only through the simultaneous use of these powerful techniques that we may ultimately hope to fully decipher the physical processes taking place on a scale of a few 0.1 au or less around young stars, indeed the birth site of the wealth of compact inner planetary systems the Kepler satellite has unveiled over the last years.

Acknowledgements. We would like to thank all the individuals who have contributed to build such a powerful instrument as GRAVITY. We thank the referees for their reports that improved the accuracy and clarity of the manuscript. This project has received funding from the European Research Council (ERC) under the European Union's Horizon 2020 research and innovation programme (grant agreement No 742095; *SPIDI*: Star-Planets-Inner Disk-Interactions, <http://www.spidi-eu.org>). This work has made use of data from the European Space Agency (ESA) mission *Gaia* (<https://www.cosmos.esa.int/gaia>), processed by the *Gaia* Data Processing and Analysis Consortium (DPAC, <https://www.cosmos.esa.int/web/gaia/dpac/consortium>). Funding for the DPAC has been provided by national institutions, in particular the institutions participating in the *Gaia* Multilateral Agreement.

References

- Alencar, S. H. P., Bouvier, J., Donati, J. F., et al. 2018, *A&A*, 620, A195
 Alencar, S. H. P., Bouvier, J., Walter, F. M., et al. 2012, *A&A*, 541, A116
 Andrews, S. M., Wilner, D. J., Espaillat, C., et al. 2011, *ApJ*, 732, 42
 Andrews, S. M., Wilner, D. J., Hughes, A. M., Qi, C., & Dullemond, C. P. 2009, *ApJ*, 700, 1502
 Anthonioz, F., Ménard, F., Pinte, C., et al. 2015, *A&A*, 574, A41
 Bouvier, J., Alencar, S. H. P., Boutelier, T., et al. 2007a, *A&A*, 463, 1017
 Bouvier, J., Alencar, S. H. P., Harries, T. J., Johns-Krull, C. M., & Romanova, M. M. 2007b, in *Protostars and Planets V*, ed. B. Reipurth, D. Jewitt, & K. Keil, 479
 Bouvier, J. & Appenzeller, I. 1992, *A&AS*, 92, 481
 Casassus, S., Avenhaus, H., Pérez, S., et al. 2018, *MNRAS*, 477, 5104
 Donati, J. F., Bouvier, J., Alencar, S. H., et al. 2019, *MNRAS*, 483, L1
 Donati, J. F., Bouvier, J., Alencar, S. H., et al. 2020, *MNRAS*, 491, 5660
 Donati, J. F., Gregory, S. G., Alencar, S. H. P., et al. 2013, *MNRAS*, 436, 881
 Eisner, J. A., Graham, J. R., Akeson, R. L., & Najita, J. 2009, *ApJ*, 692, 309
 Eisner, J. A., Hillenbrand, L. A., & Stone, J. M. 2014, *MNRAS*, 443, 1916
 Eisner, J. A., Monnier, J. D., Woillez, J., et al. 2010, *ApJ*, 718, 774
 Espaillat, C., D'Alessio, P., Hernández, J., et al. 2010, *ApJ*, 717, 441
 Gaia Collaboration, Brown, A. G. A., Vallenari, A., et al. 2018, *A&A*, 616, A1
 Gaia Collaboration, Prusti, T., de Bruijne, J. H. J., et al. 2016, *A&A*, 595, A1
 Goto, M., Carmona, A., Linz, H., et al. 2012, *ApJ*, 748, 6
 Gravity Collaboration, Abuter, R., Accardo, M., et al. 2017a, *A&A*, 602, A94
 Gravity Collaboration, Caratti o Garatti, A., Fedriani, R., et al. 2020, <https://arxiv.org/abs/2003.05404>
 Gravity Collaboration, Garcia Lopez, R., Perraut, K., et al. 2017b, *A&A*, 608, A78
 Gravity Collaboration, Perraut, K., Labadie, L., et al. 2019, *A&A*, 632, A53
 Haffert, S. Y., Bohn, A. J., de Boer, J., et al. 2019, *Nature Astronomy*, 3, 749
 Hartmann, L., Herczeg, G., & Calvet, N. 2016, *ARA&A*, 54, 135
 Kraus, S., Hofmann, K. H., Benisty, M., et al. 2008, *A&A*, 489, 1157
 Kreplin, A., Tambovtseva, L., Grinin, V., et al. 2018, *MNRAS*, 476, 4520
 Kurosawa, R. & Romanova, M. M. 2012, *MNRAS*, 426, 2901
 Kurosawa, R. & Romanova, M. M. 2013, *MNRAS*, 431, 2673
 Kurosawa, R., Romanova, M. M., & Harries, T. J. 2008, *MNRAS*, 385, 1931
 Kurosawa, R., Romanova, M. M., & Harries, T. J. 2011, *MNRAS*, 416, 2623
 Lacour, S., Dembet, R., Abuter, R., et al. 2019, *A&A*, 624, A99
 Lapeyrere, V., Kervella, P., Lacour, S., et al. 2014, *Society of Photo-Optical Instrumentation Engineers (SPIE) Conference Series*, Vol. 9146, GRAVITY data reduction software, 91462D
 Lavail, A., Kochukhov, O., Hussain, G. A. J., et al. 2017, *A&A*, 608, A77
 Lazareff, B., Berger, J. P., Kluska, J., et al. 2017, *A&A*, 599, A85
 Malbet, F., Benisty, M., de Wit, W. J., et al. 2007, *A&A*, 464, 43
 Manara, C. F., Testi, L., Natta, A., et al. 2014, *A&A*, 568, A18
 Mendigutía, I., de Wit, W. J., Oudmaijer, R. D., et al. 2015, *MNRAS*, 453, 2126
 Monnier, J. D. 2007, *New A Rev.*, 51, 604
 Muzerolle, J., Calvet, N., & Hartmann, L. 1998a, *ApJ*, 492, 743
 Muzerolle, J., Hartmann, L., & Calvet, N. 1998b, *AJ*, 116, 2965
 Najita, J., Carr, J. S., & Tokunaga, A. T. 1996, *ApJ*, 456, 292
 Pinte, C., Ménard, F., Berger, J. P., Benisty, M., & Malbet, F. 2008, *ApJ*, 673, L63
 Salyk, C., Blake, G. A., Boogert, A. C. A., & Brown, J. M. 2009, *ApJ*, 699, 330
 Salyk, C., Blake, G. A., Boogert, A. C. A., & Brown, J. M. 2011, *ApJ*, 743, 112
 van der Marel, N., van Dishoeck, E. F., Bruderer, S., et al. 2016, *A&A*, 585, A58
 Weigelt, G., Grinin, V. P., Groh, J. H., et al. 2011, *A&A*, 527, A103
 Winn, J. N., Sanchis-Ojeda, R., & Rappaport, S. 2018, *New A Rev.*, 83, 37

Appendix A: Differential observables

Figure A.1 shows the spectrally dispersed interferometric quantities for each baseline.

Appendix B: Models with azimuthal modulation

By construction, the reference of the differential phases measured across the Br γ emission line is the barycenter of the continuum emission. Given its small amplitude, a possible alternate explanation for the phase shift detected across the Br γ emission line is that the continuum emission is not exactly centered on the star, while Br γ emission is. However, any such model would be intrinsically asymmetric, because the star itself does contribute significantly to the continuum. The upper limits on the phase closures measured on the continuum define an upper limit on such an asymmetry.

Lazareff et al. (2017) implements asymmetries by means of azimuthal modulations of the circumstellar emission. Another possibility would be to shift the entire circumstellar emission with respect to the star, but this is practically indistinguishable given our limited spatial resolution. We restrict our analysis to the first terms of the modulation as defined in Lazareff et al. (2017), where the coefficient c_1 (resp. s_1) measures the flux asymmetry along the major (resp. minor) axis of the disk. We obtained upper limits of $c_1 < 0.3$ and $s_1 < 0.08$. Larger values for these parameters generate phase closure incompatible with the observations. Formally, the best asymmetric model is with $c_1 = 0.15$, $s_1 = 0$, which corresponds to a slight brightening along the major axis of the disk, towards north. This detection is, however, not significant, owing to the fact that the phase closures in the continuum are compatible with zero.

We then performed the analysis of the spectrally dispersed observations described in Sect. 3.2, but accounting for possible asymmetries in the underlying model of the continuum. Results are summarized in Table B.1. The offset of the Br γ line emitting region with respect to the center of the star indeed depends on the amount of asymmetry in the continuum, because the latter shifts the reference of the phase measurements. In summary, we conclude that the offset of the Br γ line emitting region with respect to the center of the star is affected by an additional $\pm 15 \mu\text{as}$ uncertainty when accounting for the upper limits we derive on the asymmetry of the continuum emission.

Table B.1. Best-fit offset of the Br γ line-emitting region with respect to the center of the star when accounting for azimuthal modulations in the model of the continuum.

c_1	s_1	Offset
0	0	$52 \mu\text{as}$
0.15	0	$43.6 \mu\text{as}$
0.3	0	$37.8 \mu\text{as}$
0	0.08	$48.7 \mu\text{as}$

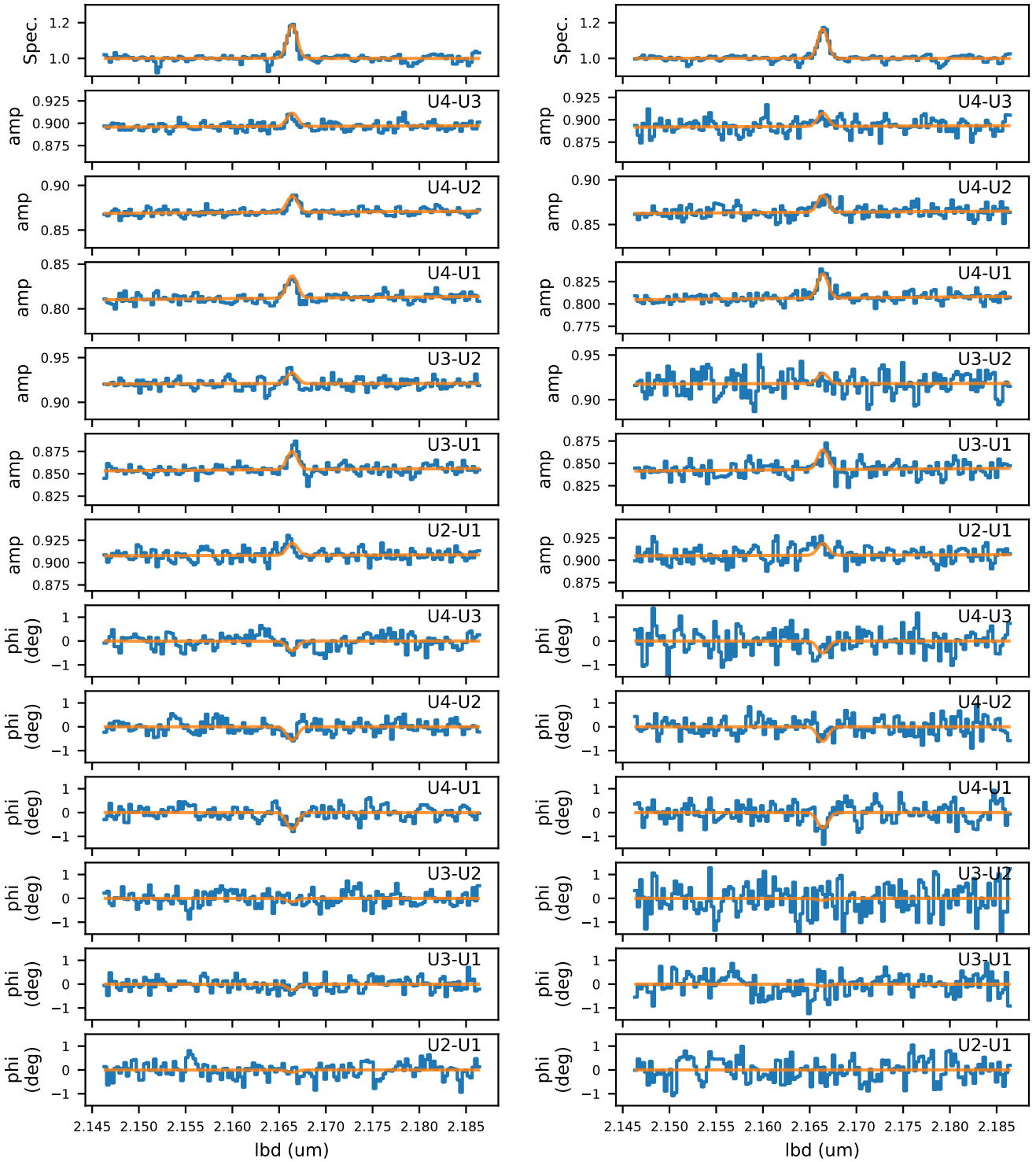


Fig. A.1. Spectrally dispersed interferometric observables around the Bry line for the night 2019-06-22 (left) and 2019-06-23 (right) along the 6 UT baselines. The top row shows the intensity spectrum where the Bry line is clearly visible in emission at $2.166 \mu\text{m}$. The next 6 rows show visibility amplitudes, and the lower 6 differential phases. For all observables, the continuum has been normalized to reproduce the predictions of the model of the FT data, and only the parameters related to the Bry emission are adjusted. The best-fit model is shown in orange.